Article

Exploring the Impact of Elements on the Reactivity of a Straightforward Procedure for Generating Vinyl-Carbazole Derivatives via a Frustrated Lewis Pair Mechanism

Zheng-Feng Zhang and Ming-Der Su*

Read Online

ACCESS | Metrics & More | Article Recommendations | SI Supporting Information

ABSTRACT: The effect of chemical element on the reactivity for carbazolation reaction of phenylacetylene utilizing $G13(C_6F_5)_3$ (Lewis acid) and G15-carbazole (Lewis base) was theoretically investigated using density functional theory (M06-2X-D3/def2-TZVP), where G13 represents Group 13 elements and G15 represents Group 15 elements. Through activation strain model (ASM) analysis, it is apparent that the reactivity of the entire carbazolation reaction is chiefly governed by the structural strain energy of the alkyne fragment. In other words, if $G13(C_6F_5)_3$ or G15-carbazole features an atomic radius that is either too small (e.g., B atom) or too large (e.g., Tl or Bi atom), it results in inadequate orbital overlap between the reactants due to the impact of steric effects. This, in turn, results in an elevation of the activation energy for such reactions, thereby impeding the alkyne from undergoing the carbazole catalytic reaction. In light of the above analyses, our theoretical findings suggest that, except for $Tl(C_6F_5)_3$, the other four Lewis acid catalysts $(B(C_6F_5)_3, Al(C_6F_5)_3, Ga((C_6F_5)_3,$ and $In((C_6F_5)_3)$ demonstrate effectiveness in catalyzing the carbazolation reaction of alkyne alongside with N-carbazole. Additionally, it is anticipated that, among the five categories of G15-carbazole molecules studied, only N-carbazole can participate in the carbazolation reaction with alkyne catalyzed by $B(C_6F_5)_3$, considering both kinetic and thermodynamic factors at room temperature. Our theoretical investigations, as outlined in this study, indicate that the carbazolation reaction of the alkyne, catalyzed by $G13(C_6F_5)_3$ and G15-carbazole, follows Hammond's postulate. To put it more plainly, when the transition state of the chemical reaction occurs earlier, it results in a decrease in activation energy.

G15-Carbazole

G13 = B, Al, Ga, In, Tl
G15 = N, P, As, Sb, Bi

G15-Vinyl Carbazole
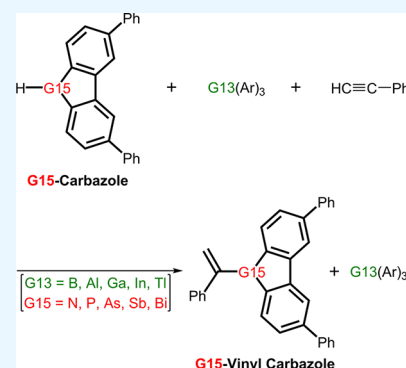
I. INTRODUCTION

Within many natural products and pharmaceuticals, carbazole emerges as a privileged heterocycle, demonstrating anti-inflammatory, antimicrobial, antioxidant, and antihistamine capabilities, as indicated in Figure 1.[1−5] Carbazole derivatives feature N-vinyl carbazoles prominently, functioning as vital building blocks for carbazole-based polymer synthesis.[6−8] These polymers are widely employed across various fields such as photovoltaics, color displays, photocopiers, solar cells, and OLEDs (Figure 1).[9−11] Thus, the growing interest in synthesizing and altering carbazoles can be attributed to their significant applications. In the past, N-vinyl carbazole derivatives were primarily obtained through the cross-coupling of N−H carbazoles with vinyl bromides, often employing palladium or copper catalysts.[12,13] Not until 2013 did Satoh's and Miura's groups devise an alternative route employing palladium-catalyzed dehydrogenative coupling of N−H carbazoles with alkenes.[14] Koenigs' group made headlines in 2020 with their report on the gold-catalyzed carbazolation reactions of alkynes.[15] Despite this, direct carbazolation reactions of alkynes without transition metals under mild conditions are still infrequent.

From 2006 onward, frustrated Lewis pair (FLP) chemistry has ignited interest in the application of boranes across a spectrum of organic transformations.[16−24] Stephan's earlier reports on the stoichiometric addition of FLPs to alkynes hold particular significance in current chemistry.[25−27] Guo, Stephan, and their colleagues have recently developed a transition metal-free catalytic carbazolation reaction of alkynes.[28] This break-through allows for the efficient synthesis of vinyl-carbazole derivatives, utilizing only 10 mol % $B(C_6F_5)_3$ as a catalyst. Through this innovative approach, researchers have success-fully prepared 24 different N-vinylcarbazole derivatives with yields varying from good to excellent.[28] It is believed that the mechanism includes the addition of the $B(C_6F_5)_3$/carbazole FLP to the alkyne, followed by proton migration resulting in the formation of the vinyl carbazole and the liberation of the borane catalyst.[28] However, to our current knowledge, there
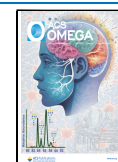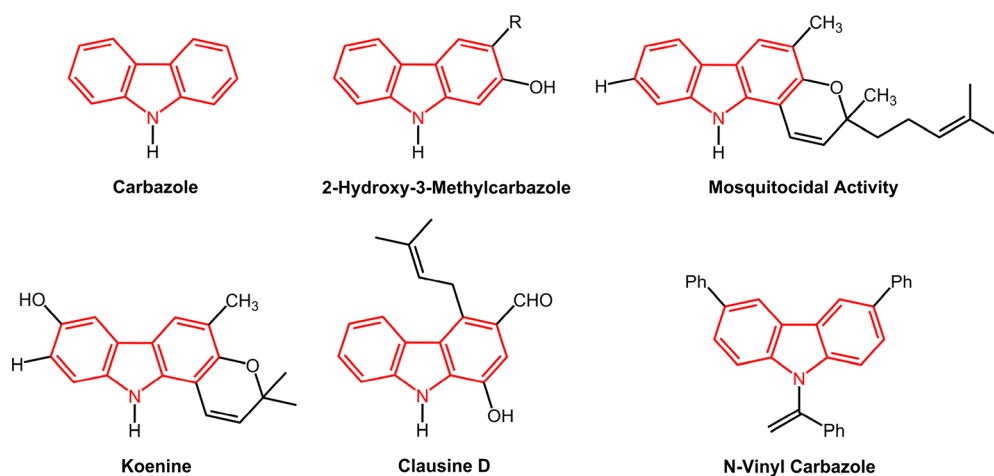
Figure 1. Some examples of carbazole-based biologically active reagents.

have been no theoretical calculations undertaken to study the reaction mechanism that leads to the formation of G15-vinyl carbazole. Additionally, the influence of diverse Group 13 (G13) or Group 15 (G15) elements on the reactivity for synthesizing G15-vinyl carbazole is still unknown. The lack of readily available experimental values and trends for such FLP catalytic reactions featuring either G13/N or B/G15 (acceptor/donor) elements underscores the critical role of computational approaches.

Here, we have selected two model reactions, each featuring either G13/N (eq 1) or B/G15 (eq 2) segments, to produce

(1)

(2)
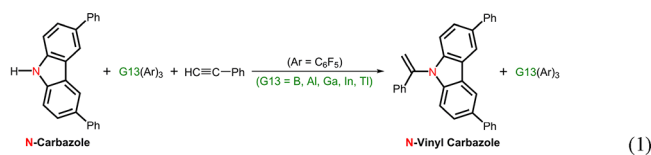
G15-based vinyl carbazole. The main objective of this study is to develop a systematic framework for understanding the factors influencing the activation barrier in these FLP catalytic reactions, thereby enabling more precise control over the entire reaction mechanism.

II. METHODOLOGY

We utilized geometry optimizations at the M06-2X[29]-D3[30−32]/def2-TZVP[33] level to ascertain the structures of stationary points along the activation pathways, which include reactants, intermediate complexes, transition states, and products. Harmonic frequency calculations were then performed to categorize the optimized structures as either minima or transition states. The selection of the M06-2X density functional, established by Zhao and Truhlar,[29] was motivated by its effectiveness in examining systems characterized by significant nonbonding interactions. Employing M06-2X-D3/def2-TZVP harmonic frequencies, we performed zero-point energy (ZPE) corrections to energies and computed thermal and entropic adjustments to free energies. Calculations

performed with the Gaussian 16 program[34] package provided thermodynamic corrections and Kohn−Sham orbitals, with all thermodynamic data referenced to a standard state of 298.15 K and 1 atm.

The activation strain model (ASM),[35−40] also recognized as the distortion/interaction model proposed by Houk and his team,[40,41,42] has proven instrumental in elucidating the underlying physical factors influencing the generation of activation barriers in different fundamental processes. Adopting the ASM, we utilize a fragment-centered methodology to comprehend chemical reactions, whereby the magnitude of reaction barriers is interpreted in relation to the initial reactants.[35−40] This systematic method extends the fragment-based approach from equilibrium structures to transition states and other nonstationary points, including those distributed along a reaction coordinate. The ASM calculations utilize optimized geometries obtained from M06-2X-D3/def2-TZVP. Incorporating relativistic effects into this single-point calculation is achieved through the application of the zero-order regular approximation (ZORA).[43−46] Consequently, this theoretical framework is identified as ZORA-M06-2X-D3/TZ2P[47]//M06-2X-D3/def2-TZVP.

Adopting the ASM, we utilize a fragment-centered methodology to comprehend chemical reactions, whereby the magnitude of reaction barriers is interpreted in relation to the initial reactants. This systematic method extends the fragment-based approach from equilibrium structures to transition states and other nonstationary points, including those distributed along a reaction coordinate. This leads to the decomposition of the potential energy surface $\Delta E(\zeta)$ along the reaction coordinate ξ into two parts: the strain $\Delta E_{strain}(\zeta)$, which relates to the deformation of the individual reactants, and the actual interaction $\Delta E_{int}(\zeta)$ between the deformed reactants:

$$\Delta E(\zeta) = \Delta E_{strain}(\zeta) + \Delta E_{int}(\zeta)$$

(3)

$\Delta E_{strain}(\zeta)$, representing strain, is determined by the rigidity of the reactants and the level of reorganization involved in a given reaction mechanism, whereas $\Delta E_{int}(\zeta)$, signifying interaction, is influenced by the electronic structure of the reactants and their orientation as they approach each other. The presence and location of a barrier along ζ are determined by the interaction between $\Delta E_{strain}(\zeta)$ and $\Delta E_{int}(\zeta)$. The activation energy of a reaction, denoted as $\Delta E^{\ddagger} = \Delta E(\zeta^{TS})$, is
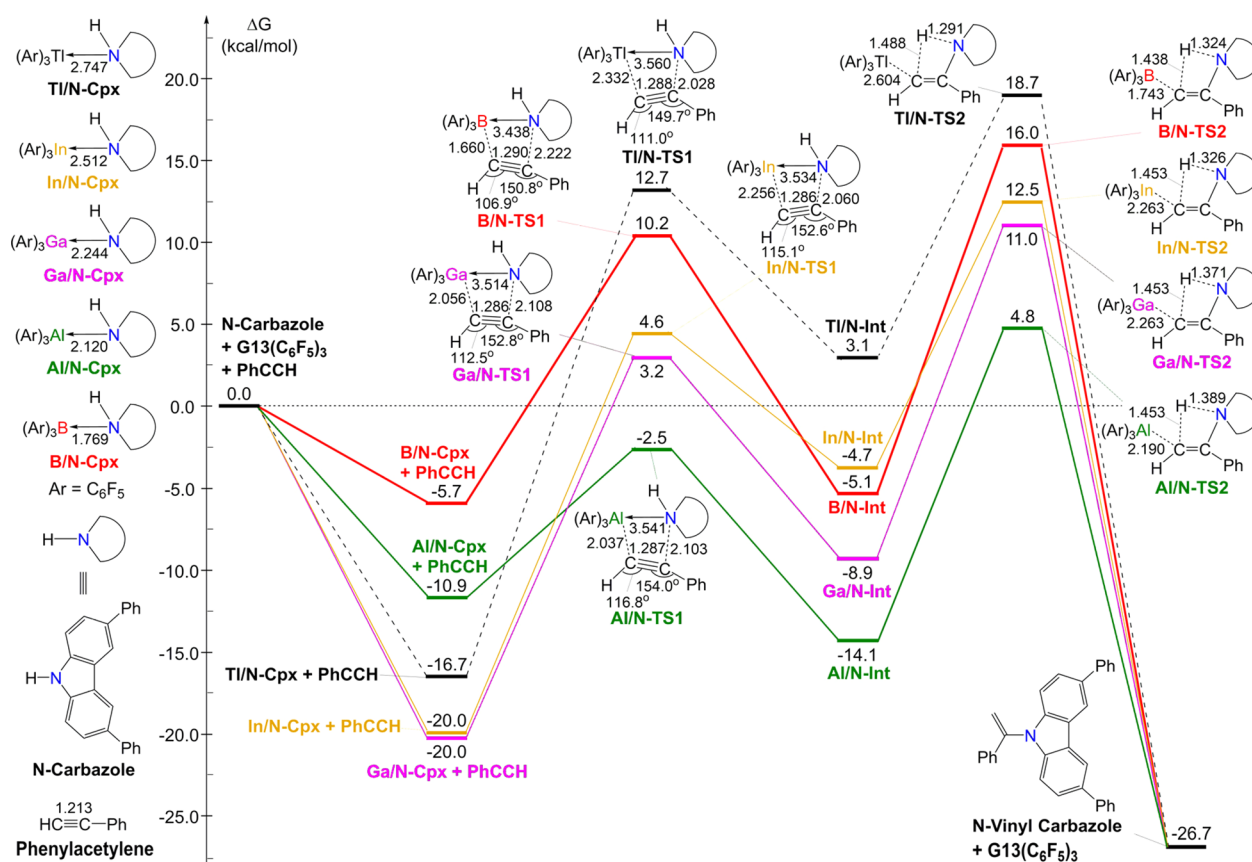
Figure 2. M06-2X-D3/def2-TZVP free energy surfaces for G13$(C_6F_5)_3$ mediated carbazolation reaction of phenylacetylene, resulting in the production of N-vinyl-carbazole and G13$(C_6F_5)_3$. Bond lengths are reported in Å, while energies are presented in kcal/mol.

composed of the activation strain $\Delta E^{\ddagger}_{strain} = \Delta E_{strain}(\zeta^{TS})$ and the transition state interaction $\Delta E^{\ddagger}_{int} = \Delta E_{int}(\zeta^{TS})$. As a result, in this work, eq 3 can be rewritten as follows:

$$\Delta E^{\ddagger} = \Delta E^{\ddagger}_{strain} + \Delta E^{\ddagger}_{int} \qquad (4)$$

III. RESULTS AND DISCUSSION

1. The Pathways of the Carbazolation Reaction Outlined in Eq 1. We initially focus on the potential energy surfaces where G13$(C_6F_5)_3$ catalyzes the reactions between carbazole and phenylacetylene (PhCCH), resulting in N−H addition to PhCCH through an FLP carbazolation mechanism (eq 1). Our computational studies indicate that in the initial stage, the lone pair of the nitrogen atom in the Lewis base (carbazole) interacts with the vacant orbital of the G13 atom in the Lewis acid (G13$(C_6F_5)_3$), leading to the formation of a precursor complex (**G13/N-Cpx**). Subsequently, phenyl-acetylene and **G13/N-Cpx** undergo a [2 + 2] cyclization reaction, resulting in the production of an intermediate (**G13/N-Int**) via the transition state **G13/N-TS1**. The acidic nature of the ammonium proton within **G13/N-Int** facilitates its migration to the carbon atom adjacent to the G13 center (**G13/N-TS2**), driving the formation of N-vinyl carbazole and releasing G13$(C_6F_5)_3$ to support subsequent catalytic processes. Thus, the pathway for the transition metal-free catalytic carbazolation reaction between PhCCH and carbazole, leading to the formation of N-vinyl-carbazole facilitated by G13$(C_6F_5)_3$, can be described as follows: N-carbazole + G13$(C_6F_5)_3$ + PhCCH → **G13/N-Cpx** + PhCCH → **G13/N-TS1** → **G13/N-Int** → **G13/N-TS2** → N-vinyl carbazole +

G13$(C_6F_5)_3$. Using the M06-2X-D3/def2-TZVP level of theory, we calculated the optimized geometries for all stationary points. Figure 2 provides an overview of the selected geometrical parameters and their relative free energies with respect to the isolated reactants. Our computations suggest that the first free activation energy of **G13/N-TS1** ($\Delta G^{\ddagger}_{G13/N-TS1}$; kcal/mol) compared to the corresponding precursor complex (**G13/N-Cpx**) increases in the following sequence: 8.4 (**Al/N-TS1**) < 15.9 (**B/N-TS1**) < 23.2 (**Ga/N-TS1**) < 24.6 (**In/N-TS1**) < 29.4 (**Tl/N-TS1**). Moreover, the second free activation energy of **G13/N-TS2** ($\Delta G^{\ddagger}_{G13/N-TS2}$; kcal/mol) relative to the corresponding intermediate (**G13/N-Int**) ranks in the order: 15.6 (**Tl/N-TS2**) < 17.2 (**In/N-TS2**) < 18.9 (**Al/N-TS2**) < 19.9 (**Ga/N-TS2**) < 21.1 (**B/N-TS2**). Reflecting on the M06-2X data provided above, it becomes clear from a kinetic standpoint that, with the sole exception of Tl$(C_6F_5)_3$, both Lewis acid (G13$(C_6F_5)_3$) and base (carba-zole) exhibit the ability to catalyze FLP reactions with PhCCH, resulting in the generation of N-vinyl carbazole at room temperature. Up until now, to the best of our awareness, experimental chemists have only reported carbazolation reactions of various alkynes mediated by B$(C_6F_5)_3$ in the absence of transition metals.[28] Thus, the conclusion derived from the preceding theoretical calculation can serve as a forecast.

The information provided in Figure 2 highlights that the first activation barrier of **G13/N-TS1** has a more substantial effect on the overall G13$(C_6F_5)_3$-mediated carbazolation reaction compared to the activation energy of **G13/N-TS2**. Hence, it is crucial for us to explore the primary factor that contributes to

the formation of the activation energy of **G13/N-TS1**. The ASM method was then applied to systematically investigate the origins of the various computed barriers for the production reaction of N-vinyl-carbazole (eq 1) via a FLP mechanism. The ASM analyses for our model reactions (eq 1) are outlined in Table 1, with computations carried out using ZORA-M06-2X-

Table 1. Activation Strain Analysis Examined the G13(C$_6$F$_5$)$_3$ Mediated Carbazolation Reaction of Phenylacetylene at the Transition State G13/N-TS1[a,b,c]

Entry	B/N-TS1	Al/N-TS1	Ga/N-TS1	In/N-TS1	Tl/N-TS1
$\Delta E^{\ddagger}$	−0.9	−23.1	−19.4	−12.0	−4.8
$\Delta E^{\ddagger}_{\text{strain,PhCCH}}$	38.3	15.8	18.5	26.3	33.9
$\Delta E^{\ddagger}_{\text{strain,G13/N-Cpx}}$	33.7	33.1	28.0	29.1	29.8
$\Delta E^{\ddagger}_{\text{int}}$	−72.9	−72.0	−65.9	−67.4	−68.5

[a]$\Delta E^{\ddagger} = \Delta E^{\ddagger}_{\text{strain,PhCCH}} + \Delta E^{\ddagger}_{\text{strain,G13/N-Cpx}} + \Delta E^{\ddagger}_{\text{int}}$ [b]All were calculated at the ZORA-M06-2X-D3/TZ2P//M06-2X-D3/def2-TZVP level. [c]All in kcal mol^{-1}.
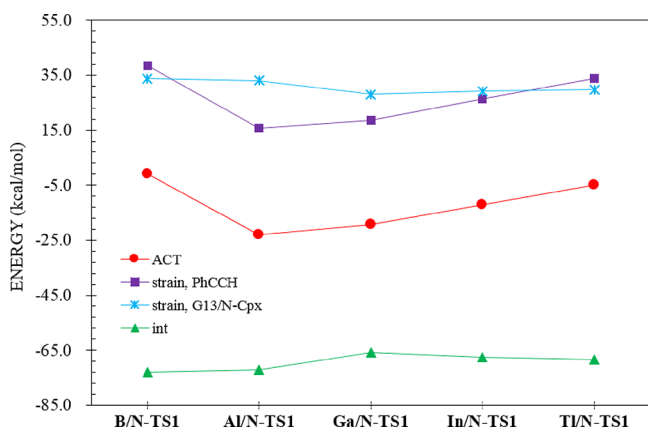
Figure 3. Energy decompositions of the activation energies ($\Delta E^{\ddagger}$) for the G13(C$_6$F$_5$)$_3$-mediated carbazolation reaction of phenylacetylene at the transition state **G13/N-TS1**, with data derived from Table 1.

D3/TZ2P//M06-2X-D3/def2-TZVP. Figure 3 provides a schematic representation of the data presented in the table. Hence, as observed in Figure 3, the activation energy ($\Delta E^{\ddagger}$) can be dissected into three terms: $\Delta E^{\ddagger} = \Delta E^{\ddagger}_{\text{strain,PhCCH}} + \Delta E^{\ddagger}_{\text{strain,G13/N-Cpx}} + \Delta E^{\ddagger}_{\text{int}}$, resulting from the distortion experienced by the isolated molecules (PhCCH and **G13/N-Cpx**) during the transformation, and the interaction energy ($\Delta E^{\ddagger}_{\text{int}}$) between the strained species along the reaction coordinate. Observations from Figure 3 indicate that $\Delta E^{\ddagger}_{\text{strain,G13/N-Cpx}}$ and $\Delta E^{\ddagger}_{\text{int}}$ remain relatively stable despite variations in the G13 element within **G13/N-TS1**. The figure clearly illustrates that the trend in the activation energies ($\Delta E^{\ddagger}$) of **G13/N-TS1** is predominantly influenced by the strain energies of PhCCH ($\Delta E^{\ddagger}_{\text{strain,PhCCH}}$). The reason for this can be attributed to the atomic size of the G13 element in LA (i.e., G13(C$_6$F$_5$)$_3$). When PhCCH is in proximity to the complex (**G13/N-Cpx**) formed by carbazole and G13(C$_6$F$_5$)$_3$, its triple bond interacts with the G13−N chemical bond of **G13/N-Cpx**, leading to a [2 + 2] cycloaddition reaction. Achieving optimal orbital overlap between the G13−N bond of **G13/N-Cpx** and the C≡C triple bond of PhCCH requires molecular structural deformation of both **G13/N-Cpx** and

PhCCH. Given its smaller molecular size, PhCCH is more easily subject to structural changes compared to **G13/N-Cpx**. Consequently, the amplitude of the strain energy curve for PhCCH ($\Delta E^{\ddagger}_{\text{strain,PhCCH}}$) exceeds that of **G13/N-Cpx** ($\Delta E^{\ddagger}_{\text{strain,G13/N-Cpx}}$). In addition, it is well accepted that the atomic radii of B and Tl are the smallest and largest respectively among the elements in Group 13.[48] In order to maximize the orbital overlap between PhCCH and **G13/N-Cpx**, the PhCCH fragment structures of **B/N-TS1** and **Tl/N-TS1** are deformed the most, resulting in their $\Delta E^{\ddagger}_{\text{strain,PhCCH}}$ being very large (Figure 3). Therefore, the activation energies of **B/N-TS1** and **Tl/N-TS1** are also larger than those of other **Al/N-TS1**, **Ga/N-TS1**, and **In/N-TS1**, as graphically represented in Figures 2 and 3.

Besides, as depicted in Figure 2, our computational analysis reveals an upward trend in the calculated C≡C bond lengths of **G13/N-TS1**: 6.0% (**Ga/N-TS1**) ∼ 6.0% (**In/N-TS1**) ∼ 6.1% (**Al/N-TS1**) < 6.2% (**Tl/N-TS1**) < 6.3% (**B/N-TS1**), relative to the initial phenylacetylene bond length of 1.213 Å. Remarkably, the elongation trend of the C≡C bond length in the PhCCH fragment geometry in **G13/N-TS1** is indicative of its associated barrier height. Additionally, in Figure 2, when considering the geometric structure of the PhCCH fragment in **G13/N-TS1**, the M06-2X computations exhibit increasing trends in the ∠H−C−C bond angles relative to 180.0° for the free PhCCH bond angle. Consequently, 36.1% (**In/N-TS1**) ∼ 36.8% (**Al/N-TS1**) < 37.5% (**Ga/N-TS1**) < 38.3% (**Tl/N-TS1**) < 40.6% (**B/N-TS1**). Similarly, the ∠C−C−Ph bond angle in these transition structures was expanded in the sequence: 14.4% (**Al/N-TS1**) < 15.1% (**Ga/N-TS1**) ∼ 15.2% (**In/N-TS1**) < 16.2% (**B/N-TS1**) < 16.8% (**Tl/N-TS1**), compared to their original PhCCH (180.0°). These findings collectively contribute to the higher activation barrier for **B/Al-TS1** and **Tl/N-TS1** during the carbazolation reaction of **G13/N-Cpx** with phenylacetylene. Furthermore, the theoretical evidence outlined above is in accordance with the Hammond postulate,[49] which posits that a transition state occurring at an earlier stage in the reaction pathway typically exhibits a lower barrier height. Therefore, our theoretical analysis proposes that the activation barrier of **G13/N-TS1** is primarily governed by the structural strain energy of the PhCCH fragment ($\Delta E^{\ddagger}_{\text{strain,PhCCH}}$) during its carbazole FLP catalytic reaction.

A thorough examination of strain energy ($\Delta E^{\ddagger}_{\text{strain}}$) in the carbazolation reaction process is facilitated by detailed ASM analysis of two representative systems: **B/N-TS1** (red) and **Tl/N-TS1** (black). Figure 4 highlights the notable similarities in ASM features between **B/N-TS1** and **Tl/N-TS1**. A detailed analysis of Figure 4 reveals that the $\Delta E^{\ddagger}_{\text{strain,PhCCH}}$ emerges as the critical determinant governing the distinct behavior of **B/N-TS1** and **Tl/N-TS1**. For instance, at the reaction coordinate 7, the calculated $\Delta E^{\ddagger}_{\text{strain,PhCCH}}$ for **B/N-TS1** and **Tl/N-TS1** amounts to 31.7 and 22.0 kcal/mol, respectively. Likewise, the computed $\Delta E^{\ddagger}_{\text{strain,B/N-Cpx}}$ for **B/N-TS1** and $\Delta E^{\ddagger}_{\text{strain,Tl/N-Cpx}}$ for **Tl/N-TS1** stand at 32.0 and 28.5 kcal/mol, whereas the estimated $\Delta E^{\ddagger}_{\text{int}}$ for **B/N-TS1** and **Tl/N-TS1** are −65.3 and −57.8 kcal/mol, respectively. Additionally, their activation energies at the same point are projected to be −1.7 and −7.2 kcal/mol, respectively. The lower barrier height for **B/N-TS1** can evidently be attributed to its diminished $\Delta E^{\ddagger}_{\text{strain,PhCCH}}$ throughout the entire reaction pathway.

2. The Pathways of the Carbazolation Reaction Outlined in Eq 2. Within this section, our attention turns to the carbazolation reaction of phenylacetylene under the
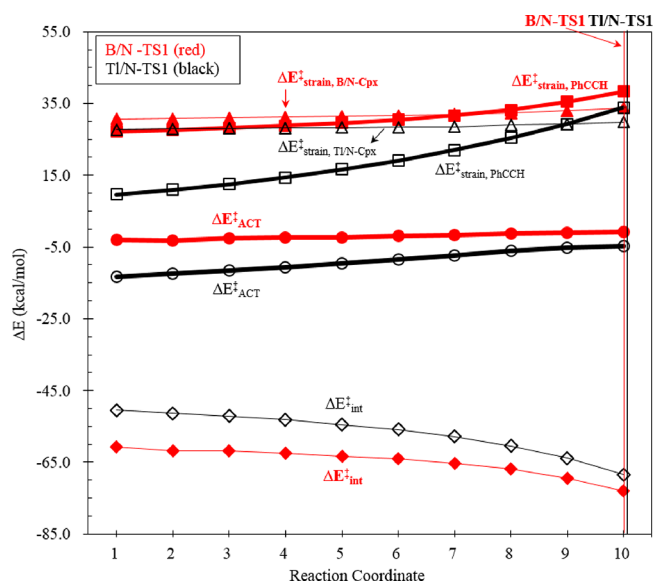
Figure 4. Presented are ASM profiles delineating the carbazolation reaction mechanism of PhCCH with N-carbazole, under the catalysis of both $B(C_6F_5)_3$ (red) and $Tl(C_6F_5)_3$ (red). The two transition states under consideration are **B/N-TS1** and **Tl/N-TS1**, respectively. These profiles are graphed as a function of the reaction coordinate, specifically in relation to the $C\equiv C\cdots N$ distance. The computational data utilized for constructing these profiles were obtained at the ZORA-M06-2X-D3/TZ2P//M06-2X-D3/def2-TZVP level.

influence of $B(C_6F_5)_3$, producing G15-vinyl-carbazole and $B(C_6F_5)_3$, as indicated in eq 2. Parallel to the carbazolation reaction outlined in eq 1, we anticipate that the activation process of PhCCH involving G15-carbazole and $B(C_6F_5)_3$, investigated in this study, follows a comparable reaction pathway: G15-carbazole + $B(C_6F_5)_3$ + PhCCH → **B/G15-Cpx** + PhCCH → **B/G15-TS1** → **B/G15-Int** → **B/G15-TS2** → G15-vinyl carbazole + $B(C_6F_5)_3$. The potential energy profiles, analyzed using the M06-2X-D3/def2-TZVP level of theory, are illustrated in Figure 5.

In the given scenario, two transition states are observed: **B/G15-TS1** and **B/G15-TS2**. The free activation energy of the former $(\Delta G^{\ddagger}_{B/G15-TS1};$ kcal/mol), computed relative to its corresponding **B/G15-Cpx**, demonstrates an increasing trend: 11.0 (**B/Al-TS1**) < 13.7 (**B/As-TS1**) < 15.9 (**B/N-TS1**) < 17.6 (**B/Sb-TS1**) < 29.5 (**B/Bi-TS1**). Conversely, the free activation energy of the latter $(\Delta G^{\ddagger}_{B/G15-TS2};$ kcal/mol), compared to its corresponding **B/G15-Int**, shows a similar ascending pattern: 21.1 (**B/N-TS2**) < 35.1 (**B/Bi-TS2**) < 39.5 (**B/Sb-TS2**) < 40.6 (**B/As-TS2**) < 43.3 (**B/P-TS2**). Analyzing the data shown in Figure 5, it becomes apparent that the pivotal transition state determining the carbazolation reaction of PhCCH by G15-carbazole is the second transition state (**B/G15-TS2**), not the initial transition state (**B/G15-TS1**). This means that the second activation barrier of **B/G15-TS2** holds more significance in regulating the overall $B(C_6F_5)_3$-mediated carbazolation reaction than the activation barrier of **B/G15-TS1**. This observation contrasts with the computational outcomes illustrated in the preceding Figure 2, where the primary transition state for the carbazolation reaction of PhCCH facilitated by the Lewis acid $G13(C_6F_5)_3$ is the first transition state, **G13/N-TS1**, as opposed to the second transition state (**G13/N-TS2**). Therefore, according to our M06-2X results presented in Figure 5, it is suggested that,

considering both kinetic and thermodynamic factors at room temperature, only N-carbazole and PhCCH is a viable candidate for undergoing the carbazolation reaction catalyzed by the Lewis acid $B(C_6F_5)_3$. The validity of this theoretical prediction has been supported by available chemical experiments conducted by Guo, Stephan, and their research group.[28]

To ensure alignment with the ASM discussion presented earlier (i.e., Table 1 and Figure 3) for eq 1, we employ ASM to investigate the origin of the first activation energy in eq 2. This enables a clearer comprehension of the fundamental factor driving the carbazole reaction using the Lewis acid $(B(C_6F_5)_3)$ and base (G15-carbazole). Table 2 provides a detailed account of the activation strain analyses for our model reactions (eq 2), computed using ZORA-M06-2X-D3/TZ2P//M06-2X-D3/def2-TZVP. Figure 6 offers a graphical representation of the tabulated information. According to the findings in Figure 6, $\Delta E^{\ddagger}_{strain,B/G15-Cpx}$ and $\Delta E^{\ddagger}_{int}$ show little variation among different **B/G15-TS1** instances. However, the barrier heights of **B/G15-TS1** are mainly dictated by the strain energy of PCCH $(\Delta E^{\ddagger}_{strain,PhCCH})$. This pattern can also be explained by the atomic size of the G15 element in LB (i.e., G15-carbazole). As PhCCH approaches the complex (**B/G15-Cpx**), consisting of G15-carbazole and $B(C_6F_5)_3$, the B−G15 chemical bond of **B/G15-Cpx** initiates interaction with the $C\equiv C$ triple bond of PhCCH, triggering a $[2 + 2]$ cycloaddition reaction. Molecular structural deformations of both **B/G15-Cpx** and PhCCH are essential for achieving optimal orbital overlap between the B−G15 bond of **B/G15-Cpx** and the $C\equiv C$ triple bond of PhCCH. The smaller molecular size of PhCCH facilitates its structural changes in comparison to **B/G15-Cpx**, resulting in a larger amplitude of the strain energy curve for PhCCH $(\Delta E^{\ddagger}_{strain,PhCCH})$ compared to **B/G15-Cpx** $(\Delta E^{\ddagger}_{strain,B/G15-Cpx})$, as schematically represented in Figure 6. Moreover, among the Group 15 elements, N and Bi possess the smallest and largest atomic radii, respectively.[48] To maximize the overlap between the $C\equiv C$ triple bond of PhCCH and the B−G15 bond of **B/G15-Cpx**, the geometric structure of PhCCH must be extensively deformed. As a consequence, the heightened $\Delta E^{\ddagger}_{strain,PhCCH}$ within **B/N-TS1** and **B/Bi-TS1** leads to higher activation energies for these transition states compared to counterparts like **B/P-TS1**, **B/As-TS1**, and **B/Sb-TS1**, as schematically illustrated in Figures 5 and 6.

Indeed, upon reviewing the computed geometrical parameters from Figure 5, it is clear that the $C\equiv C$ bond length in **B/G15-TS1** follows a pattern: 4.9% (**B/P-TS1**) < 5.4% (**B/As-TS1**) < 5.5% (**B/Sb-TS1**) < 6.3% (**B/N-TS1**) < 8.4% (**B/Bi-TS1**), relative to the unbound phenylacetylene (1.213 Å). Additionally, the $\angle H−C−C$ bond angle in the **B/G15-TS1** transition state experiences an increase in the order of 37.6% (**B/P-TS1**) < 37.9% (**B/As-TS1**) < 38.1% (**B/Sb-TS1**) < 38.3% (**B/Bi-TS1**) < 40.6% (**B/N-TS1**), compared to the original PhCCH bond angle of 180.0°. Similarly, the $\angle C−C−Ph$ bond angle in the **B/G15-TS1** structure is elevated in the sequence of 6.3% (**B/P-TS1**) < 8.3% (**B/As-TS1**) < 9.3% (**B/Sb-TS1**) < 15.6% (**B/Bi-TS1**) < 16.2% (**B/N-TS1**), relative to its isolated PhCCH bond angle of 180.0°. Accordingly, the theoretical examinations outlined above yield an interesting observation: when the G15-carbazole molecule acts as the Lewis base, with either nitrogen or bismuth at the LB center, it exhibits a later transition state with the highest energy barrier during its interaction with $B(C_6F_5)_3$ (as the Lewis acid) in the carbazolation reaction with PhCCH. By contrast, G15-carbazole molecules with other heavy group 15 elements (P-
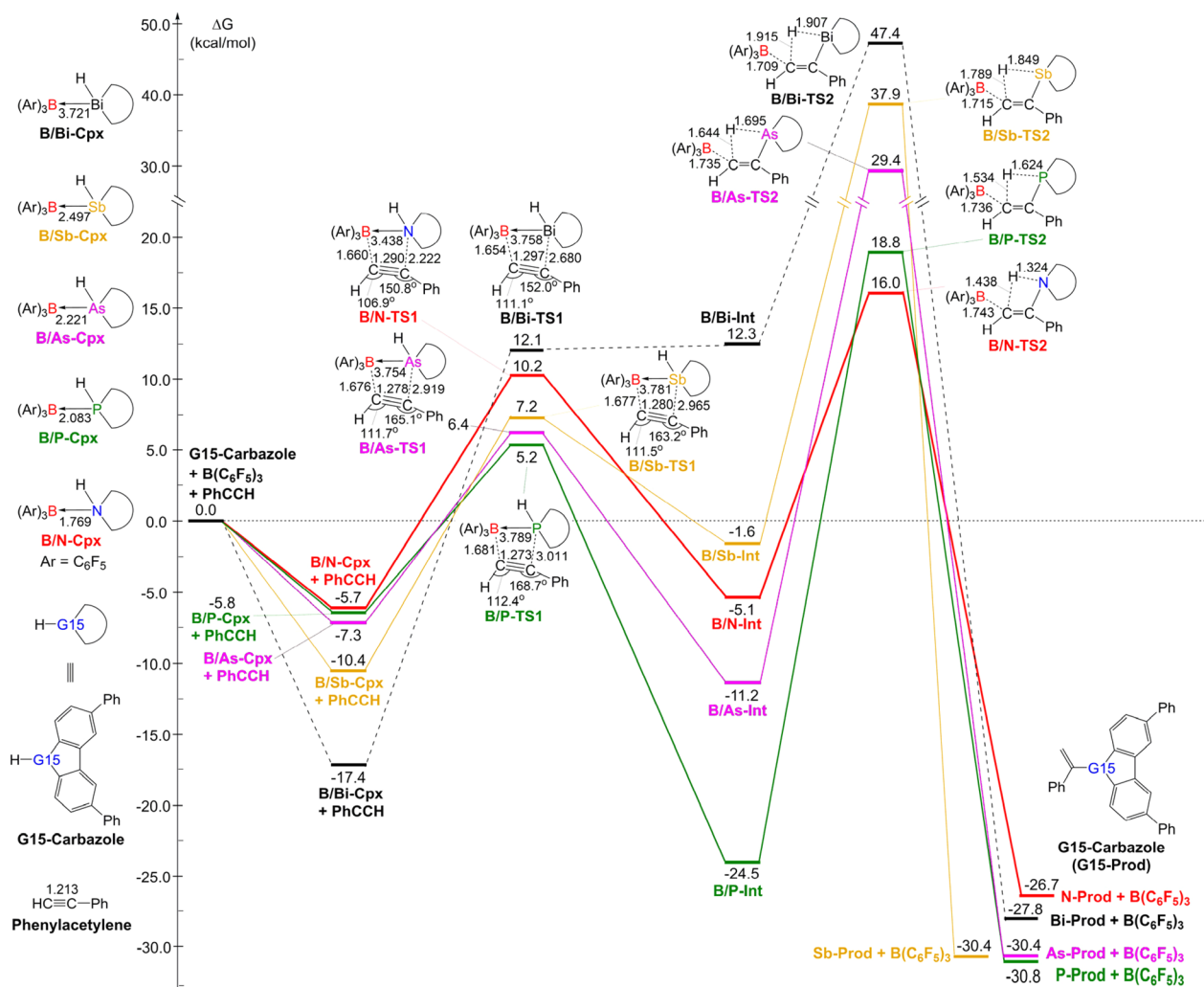
Figure 5. M06-2X-D3/def2-TZVP free energy surfaces for $B(C_6F_5)_3$ mediated carbazolation reaction of phenylacetylene, resulting in the production of G15-vinyl-carbazole and $B(C_6F_5)_3$. Bond lengths are reported in Å, while energies are presented in kcal/mol.

Table 2. Activation Strain Analysis Examined the $B(C_6F_5)_3$-Mediated Carbazolation Reaction of Phenylacetylene at the Transition State B/G15-TS1[a,b,c]

Entry	B/N-TS1	B/P-TS1	B/As-TS1	B/Sb-TS1	B/Bi-TS1
$\Delta E^{\ddagger}$	−0.9	−18.7	−12.2	−10.1	−8.5
$\Delta E^{\ddagger}_{strain,PhCCH}$	38.3	16.2	18.4	23.6	33.4
$\Delta E^{\ddagger}_{strain,B/G15-Cpx}$	33.7	31.6	38.0	36.5	37.9
$\Delta E^{\ddagger}_{int}$	−72.9	−66.5	−68.6	−70.2	−79.8

[a] $\Delta E^{\ddagger} = \Delta E^{\ddagger}_{strain,PhCCH} + \Delta E^{\ddagger}_{strain,B/G15-Cpx} + \Delta E^{\ddagger}_{int}$ [b] All were calculated at the ZORA-M06-2X-D3/TZ2P//M06-2X-D3/def2-TZVP level. [c] All in kcal mol^{-1}.

carbazole, As-carbazole, and Sb-carbazole) as the LB center tend to manifest transition states that are relatively earlier and have lower activation barriers. Therefore, the theoretical observations discussed above might be explained by the presence of transition states resembling products and reactants, respectively, aligning with the Hammond postulate.[49]

Similarly, by employing the ASM approach again, we singled out two representative transition states, **B/N-TS1** and **B/Bi-TS1**, for further analysis. Figure 7 reveals that at reaction coordinate 7, the $\Delta E^{\ddagger}_{strain,PhCCH}$ for transition states is 31.7 (**B/N-TS1**) and 28.1 (**B/N-TS1**) kcal/mol, respectively. Con-
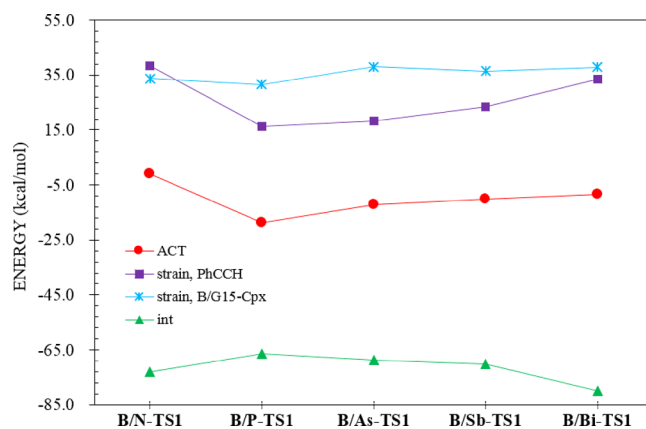
Figure 6. Energy decompositions of the activation energies ($\Delta E^{\ddagger}$) for the G13$(C_6F_5)_3$-mediated carbazolation reaction of phenylacetylene at the transition state **B/15-TS1**, with data derived from Table 2.

versely, their $\Delta E^{\ddagger}_{strain,B/G15-Cpx}$ is estimated at 32.0 and 36.7 kcal/mol, with their $\Delta E^{\ddagger}_{int}$ standing at −65.3 and −73.7 kcal/mol, respectively. With its smaller atomic radius, the nitrogen atom (LB) in N-carbazole can undergo significant distortion to reach the transition state (**B/N-TS1**), resulting in a higher $\Delta E^{\ddagger}_{strain,PhCCH}$. Consequently, a greater $\Delta E^{\ddagger}$ (−1.6 kcal/mol) is
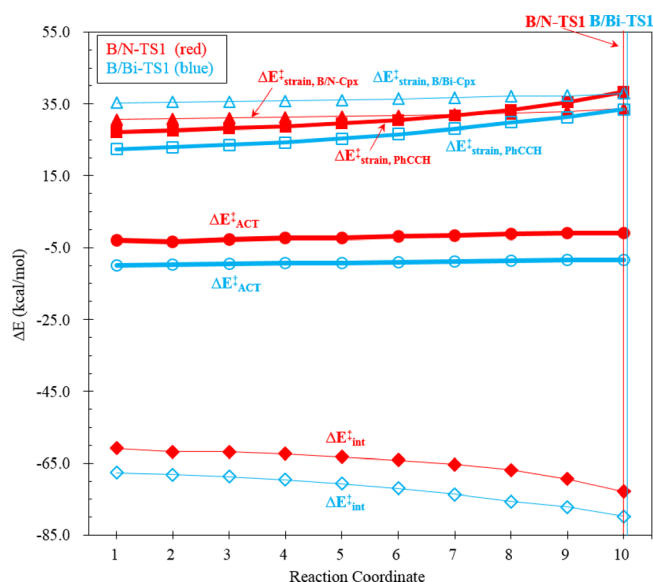
Figure 7. ASM profiles delineating the carbazolation reaction mechanism of PhCCH with G15-carbazole, under the catalysis of $B(C_6F_5)_3$. The two transition states under consideration are **B/N-TS1** (red) and **B/Bi-TS1** (blue), respectively. These profiles are graphed as a function of the reaction coordinate, specifically in relation to the C≡C···G15 distance. The computational data utilized for constructing these profiles were obtained at the ZORA-M06-2X-D3/TZ2P// M06-2X-D3/def2-TZVP level.

achieved. In contrast, the transition state **B/Bi-TS-1** exhibits a smaller $\Delta E^{\ddagger}_{\text{strain,PhCCH}}$, leading to a smaller $\Delta E^{\ddagger}$ (−8.9 kcal/ mol). Thus, the computational results in Figure 7 clarify that the difference in the activation barrier $\Delta E^{\ddagger}$ primarily arises from the contribution of $\Delta E^{\ddagger}_{\text{strain,PhCCH}}$.

IV. CONCLUSIONS

The current study highlights several important findings.

(1) Our theoretical analyses reveal that, except for Tl-$(C_6F_5)_3$, the other four Lewis acid catalysts $(B(C_6F_5)_3,$ $Al(C_6F_5)_3,$ $Ga(C_6F_5)_3,$ and $In(C_6F_5)_3)$ are proficient in catalyzing the carbazolation reaction of PhCCH alongside with N-carbazole, resulting in the formation of N-vinyl-carbazole and $G13(C_6F_5)_3$, considering both kinetic and thermodynamic factors.

(2) Based on our M06-2X results, it is evident that, among the five categories of Lewis base G15-carbazole molecules investigated, only N-carbazole can engage in the carbazolation reaction with PhCCH catalyzed by the Lewis acid $B(C_6F_5)_3$, considering both kinetic and thermodynamic factors at room temperature.

(3) By employing ASM, our theoretical examination indicates that the activation barrier associated with the carbazolation reaction of PhCCH with G15-carbazole as the Lewis base, catalyzed by $G13(C_6F_5)_3$ as the Lewis acid to yield G15-vinyl-carbazole and $G13(C_6F_5)_3$, is predominantly determined by the structural strain energy of the PhCCH fragment $(\Delta E^{\ddagger}_{\text{strain,PhCCH}})$ during the FLP catalytic process. In other words, when $G13(C_6F_5)_3$ or G15-carbazole possesses an atomic radius that is either too small (like the B atom) or too large (such as the Tl or Bi atom), it leads to deficient orbital overlap between the reactants due to the influence of steric effects. This causes the activation

energy of such reactions to rise, rendering it impossible for PhCCH to participate in the carbazole FLP catalytic reaction.

(4) Analysis of the reaction mechanism clarifies that the carbazole FLP catalytic reaction consists of two transition states: the initial [2 + 2] cyclization reaction between **G13/G15-Cpx** and PhCCH, followed by the transfer reaction of a proton with acidic nature. Our theoretical observations suggest that in the $G13(C_6F_5)_3$-mediated carbazolation reaction of PhCCH, the first transition state (**G13/N-TS1**) is crucial for determining this FLP catalytic reaction. Conversely, in the reaction involving $B(C_6F_5)_3$-mediated carbazolation of PhCCH with G15-carbazole, it is the second transition state (**B/ G15-TS2**) that plays a pivotal role in determining its FLP-catalyzed reaction.

(5) Our theoretical investigations outlined in this study suggest that the carbaolation reaction of PhCCH by $G13(C_6F_5)_3$ (Lewis acid) and G15-carbazole (Lewis base) follows Hammond's postulate. In simpler terms, when the transition state of the chemical reaction appears earlier, the activation energy decrease.

■ ASSOCIATED CONTENT

ⓢ Supporting Information

The Supporting Information is available free of charge at https://pubs.acs.org/doi/10.1021/acsomega.4c05298.

The optimized geometries for all stationary points (**G13/N-Rea, G13/N-Cpx, G13/N-TS1, G13/N-Int, G13/N-TS2, G13(C_6F_5)_3, B/G15-Rea, B/G15-Cpx, B/ G15-TS1, B/G15-Int, B/G15-TS2,** and **G15-Prod**) calculated at the M06-2X-D3/def2-TZVP level of theory (PDF)

■ AUTHOR INFORMATION

Corresponding Author

Ming-Der Su − *Department of Applied Chemistry, National Chiayi University, Chiayi 60004, Taiwan; Department of Medicinal and Applied Chemistry, Kaohsiung Medical University, Kaohsiung 80708, Taiwan;* ⓞ orcid.org/0000-0002-5847-4271; Email: midesu@mail.ncyu.edu.tw

Author

Zheng-Feng Zhang − *Department of Applied Chemistry, National Chiayi University, Chiayi 60004, Taiwan*

Complete contact information is available at:
https://pubs.acs.org/10.1021/acsomega.4c05298

Author Contributions

Z.-F. Zhang conducted all of the theoretical computations and analyzed the results. M.-D. Su supervised the research activities and contributed to the manuscript preparation. The two authors regularly discussed the progress of the research, reviewed the manuscript, and gave approval for the final version.

Notes

The authors declare no competing financial interest.

■ ACKNOWLEDGMENTS

■ REFERENCES

(1) Knölker, H.-J.; Reddy, K. R. Isolation and Synthesis of Biologically Active Carbazole Alkaloids. *Chem. Rev.* **2002**, *102*, 4303−4427.

(2) Schmidt, A. W.; Reddy, K. R.; Knölker, H.-J. Occurrence, Biogenesis, and Synthesis of Biologically Active Carbazole Alkaloids. *Chem. Rev.* **2012**, *112*, 3193−3328.

(3) Ramsewak, R. S.; Nair, M. G.; Strasburg, G. M.; DeWitt, D. L.; Nitiss, J. L. Biologically Active Carbazole Alkaloids from Murraya koenigii. *J. Agric. Food Chem.* **1999**, *47*, 444−447.

(4) Tachibana, Y.; Kikuzaki, H.; Lajis, N. H.; Nakatani, N. Antioxidative Activity of Carbazoles from Murraya koenigii Leaves x. *J. Agric. Food Chem.* **2001**, *49*, 5589−5594.

(5) Takeda, D.; Hirano, K.; Satoh, T.; Miura, M. Synthesis of N-Vinylcarbazoles via Dehydrogenative Coupling of N-H Carbazoles with Alkenes under Palladium Catalysis. *Org. Lett.* **2013**, *15*, 1242−1245.

(6) Jana, S.; He, F.; Koenigs, R. M. Gold-Catalyzed Carbazolation Reactions of Alkynes. *Org. Lett.* **2020**, *22*, 4873−4877.

(7) Blouin, N.; Leclerc, M. Poly(2,7-carbazole)s: Structure-Property Relationships. *Acc. Chem. Res.* **2008**, *41*, 1110−1119.

(8) Li, J.; Grimsdale, A. C. Carbazole-based polymers for organic photovoltaic devices. *Chem. Soc. Rev.* **2010**, *39*, 2399−2410.

(9) Huang, C.-F.; Hsieh, Y.-A.; Hsu, S.-C.; Matyjaszewski, K. Synthesis of poly(N-vinyl carbazole)-based block copolymers by sequential polymerizations of RAFT-ATRP. *Polymer* **2014**, *55*, 6051−6057.

(10) Garg, V.; Kumar, P.; Verma, A. K. Substrate-Controlled Regio- and Stereoselective Synthesis of (Z)- and (E)-N-Styrylated Carbazoles, Aza-carbazoles, and γ-Carbolines via Hydroamination of Alkynes. *J. Org. Chem.* **2018**, *83*, 11686−11702.

(11) Verma, A. K.; Joshi, M.; Singh, V. P. Base-Mediated Regio- and Stereoselective Intermolecular Addition of Alkynes to N-Hetero-cycles. *Org. Lett.* **2011**, *13*, 1630−1633.

(12) Lebedev, A. Y.; Izmer, V. V.; Kazyul'kin, D. N.; Beletskaya, I. P.; Voskoboynikov, A. Z. Palladium-Catalyzed Stereocontrolled Vinyl-ation of Azoles and Phenothiazine. *Org. Lett.* **2002**, *4*, 623−626.

(13) Hirano, K.; Inaba, Y.; Takahashi, N.; Shimano, M.; Oishi, S.; Fujii, N.; Ohno, H. Direct Synthesis of Fused Indoles by Gold-Catalyzed Cascade Cyclization of Diynes. *J. Org. Chem.* **2011**, *76*, 1212−1227.

(14) Takeda, D.; Hirano, K.; Satoh, T.; Miura, M. Synthesis of N-Vinylcarbazoles via Dehydrogenative Coupling of N-H Carbazoles with Alkenes under Palladium Catalysis. *Org. Lett.* **2013**, *15*, 1242−1245.

(15) Jana, S.; He, F.; Koenigs, R. M. Gold-Catalyzed Carbazolation Reactions of Alkynes. *Org. Lett.* **2020**, *22*, 4873−4877.

(16) Dureen, M. A.; Stephan, D. W. Terminal Alkyne Activation by Frustrated and Classical Lewis Acid/Phosphine Pairs. *J. Am. Chem. Soc.* **2009**, *131*, 8396−8398.

(17) Stephan, D. W.; Erker, G. Frustrated Lewis Pairs: Metal-free Hydrogen Activation and More. *Angew. Chem., Int. Ed.* **2010**, *49*, 46−76.

(18) Stephan, D. W. Frustrated Lewis Pairs. *J. Am. Chem. Soc.* **2015**, *137*, 10018−10032.

(19) Stephan, D. W. Frustrated Lewis Pairs: From Concept to Catalysis. *Acc. Chem. Res.* **2015**, *48*, 306−316.

(20) Chan, J. Z.; Yao, W.; Hastings, B. T.; Lok, C. K.; Wasa, M. Direct Mannich-Type Reactions Promoted by Frustrated Lewis Acid/Brønsted Base Catalysts. *Angew. Chem., Int. Ed.* **2016**, *55*, 13877−13881.

(21) Stephan, D. W. The broadening reach of frustrated Lewis pair chemistry. *Science* **2016**, *354*, aaf7229.

(22) Shang, M.; Wang, X. X.; Koo, S. M.; Youn, J.; Chan, J. Z.; Yao, W. Z.; Hastings, B. T.; Wasa, M. Frustrated Lewis Acid/Brønsted Base Catalysts for Direct Enantioselective α-Amination of Carbonyl Compounds. *J. Am. Chem. Soc.* **2017**, *139*, 95−98.

(23) Jupp, A. R.; Stephan, D. W. New Directions for Frustrated Lewis Pair Chemistry. *Trends in Chemistry* **2019**, *1*, 35−48.

(24) Stephan, D. W. Catalysis, FLPs, and Beyond. *Chem.* **2020**, *6*, 1520−1526.

(25) Shang, M.; Cao, M.; Wang, Q. F.; Wasa, M. Enantioselective Direct Mannich-Type Reactions Catalyzed by Frustrated Lewis Acid/Brønsted Base Complexes. *Angew. Chem., Int. Ed.* **2017**, *56*, 13338−13341.

(26) Dureen, M. A.; Brown, C. C.; Stephan, D. W. Addition of Enamines or Pyrroles and $B(C_6F_5)_3$ "Frustrated Lewis Pairs" to Alkynes. *Organometallics* **2010**, *29*, 6422−6432.

(27) Mahdi, T.; Stephan, D. W. Stoichiometric and Catalytic Inter- and Intramolecular Hydroamination of Terminal Alkynes by Frustrated Lewis Pairs. *Chem.—Eur. J.* **2015**, *21*, 11134−11142.

(28) Zhao, Y.; Jin, L.; Guo, J.; Stephan, D. W. Catalytic hydroaminations of alkynes: a facile protocol to vinyl-carbazole derivatives via a frustrated Lewis pair mechanism. *Chem. Commun.* **2022**, *58*, 3039−3042.

(29) Zhao, Y.; Truhlar, D. G. Exploring the Limit of Accuracy of the Global Hybrid Meta Density Functional for Main-Group Thermo-chemistry, Kinetics, and Noncovalent Interactions. *J. Chem. Theory Comput.* **2008**, *4*, 1849−1868.

(30) Grimme, S.; Antony, J.; Ehrlich, S.; Krieg, H. A consistent and accurate ab initio parametrization of density functional dispersion correction (DFT-D) for the 94 elements H-Pu. *J. Chem. Phys.* **2010**, *132*, 154104−154122.

(31) Grimme, S.; Ehrlich, S.; Goerigk, L. Effect of the Damping Function in Dispersion Corrected Density Functional Theory. *J. Comput. Chem.* **2011**, *32*, 1456−1465.

(32) Smith, D. G. A.; Burns, L. A.; Patkowski, K.; Sherrill, C. D. Revised Damping Parameters for the D3 Dispersion Correction to Density Functional Theory. *J. Phys. Chem. Lett.* **2016**, *7*, 2197−2203.

(33) Weigend, F. Accurate Coulomb-fitting basis sets for H to Rn. *Phys. Chem. Chem. Phys.* **2006**, *8*, 1057−1065.

(34) Frisch, M. J.; Trucks, G. W.; Schlegel, H. B.; Scuseria, G. E.; Robb, M. A.; Cheeseman, J. R.; Scalmani, G.; Barone, V.; Mennucci, B.; Petersson, G. A.; Nakatsuji, H.; Caricato, M.; Li, X.; Hratchian, H. P.; Izmaylov, A. F.; Bloino, J.; Zheng, G.; Sonnenberg, J. L.; Hada, M.; Ehara, M.; Toyota, K.; Fukuda, R.; Hasegawa, J.; Ishida, M.; Nakajima, T.; Honda, Y.; Kitao, O.; Nakai, H.; Vreven, T.; Montgomery, J. A., Jr; Peralta, J. E.; Ogliaro, F.; Bearpark, M.; Heyd, J. J.; Brothers, E.; Kudin, K. N.; Staroverov, V. N.; Keith, T.; Kobayashi, R.; Normand, J.; Raghavachari, K.; Rendell, A.; Burant, J. C.; Iyengar, S. S.; Tomasi, J.; Cossi, M.; Rega, N.; Millam, J. M.; Klene, M.; Knox, J. E.; Cross, J. B.; Bakken, V.; Adamo, C.; Jaramillo, J.; Gomperts, R.; Stratmann, R. E.; Yazyev, O.; Austin, A. J.; Cammi, R.; Pomelli, C.; Ochterski, J. W.; Martin, R. L.; Morokuma, K.; Zakrzewski, V. G.; Voth, G. A.; Salvador, P.; Dannenberg, J. J.; Dapprich, S.; Daniels, A. D.; Farkas, O.; Foresman, J. B.; Ortiz, J. V.; Cioslowski, R. L.; Martin, K.; Morokuma, Ö.; Farkas, J. B.; Foresman, D. J. F. *Gaussian 16*, revision C.01; Gaussian, Inc.: Wallingford, CT, 2016.

(35) Bickelhaupt, F. M. Understanding Reactivity with Kohn- Sham Molecular Orbital Theory: E2-S(N)2 Mechanistic Spectrum and Other Concepts. *J. Comput. Chem.* **1999**, *20*, 114−128.

(36) van Zeist, W.-J.; Bickelhaupt, F. M. The Activation Strain Model of Chemical Reactivity. *Org. Biomol. Chem.* **2010**, *8*, 3118−3127.

(37) Fernández, I.; Bickelhaupt, F. M. The activation strain model and molecular orbital theory: understanding and designing chemical reactions. *Chem. Soc. Rev.* **2014**, *43*, 4953−4967.

(38) Fernández, I. Combined activation strain model and energy decomposition analysis methods: a new way to understand pericyclic reactions. *Phys. Chem. Chem. Phys.* **2014**, *16*, 7662−7671.

(39) Wolters, L. P.; Bickelhaupt, F. M. *WIREs Comput. Mol. Sci.* **2015**, *5*, 324−343.

(40) Fernández, I. In *Discovering the Future of Molecular Sciences*; Pignataro, B., Ed.; Wiley-VCH: Weinheim, 2014; pp 165−187.

(41) Ess, D. H.; Houk, K. N. Distortion/Interaction Energy Control of 1,3-Dipolar Cycloaddition Reactivity. *J. Am. Chem. Soc.* **2007**, *129*, 10646−10647.

(42) Ess, D. H.; Houk, K. N. Theory of 1,3-Dipolar Cycloadditions: Distortion/Interaction and Frontier Molecular Orbital Models. *J. Am. Chem. Soc.* **2008**, *130*, 10187−10198.

(43) Ess, D. H.; Jones, G. O.; Houk, K. N. Transition States of Strain-Promoted Metal-Free Click Chemistry: 1,3-Dipolar Cyclo-additions of Phenyl Azide and Cyclooctynes. *Org. Lett.* **2008**, *10*, 1633−1636.

(44) Chang, Ch.; Pelissier, M.; Durand, Ph. Regular Two-Component Pauli-Like Effective Hamiltonians in Dirac Theory. *Phys. Scr.* **1986**, *34*, 394−404.

(45) Heully, J -L; Lindgren, I; Lindroth, E; Lundqvist, S; Martensson-Pendrill, A -M Diagonalisation of the Dirac Hamiltonian as a basis for a relativistic many-body procedure. *J. Phys. B* **1986**, *19*, 2799−2815.

(46) Mitoraj, M.; Michalak, A. Natural Orbitals for Chemical Valence as Descriptors of Chemical Bonding in Transition Metal Complexes. *J. Mol. Model.* **2007**, *13*, 347−355.

(47) van Lenthe, E.; Baerends, E. J. Optimized Slater-type basis sets for the elements 1−118. *J. Comput. Chem.* **2003**, *24*, 1142−1156.

(48) Cordero, B.; Gómez, V.; Platero-Prats, A. E.; Revés, M.; Echeverría, J.; Cremades, E.; Barragán, F.; Alvarez, S. Covalent radii revisited. *Dalton Trans.* **2008**, *37*, 2832−2838.

(49) Hammond, G. S. A Correlation of Reaction Rates. *J. Am. Chem. Soc.* **1955**, *77*, 334−338.